The variation of the velocity and turbulent kinetic energy field in the wave in the vicinity of the breaking point

Toomas Liiv[a] and Priidik Lagemaa[b]

[a] Department of Mechanics, Tallinn University of Technology, Ehitajate tee 5, 19086 Tallinn, Estonia; toomas@corson.ee
[b] Marine Systems Institute, Tallinn University of Technology, Akadeemia tee 21, 12618 Tallinn, Estonia; priidik26@gmail.com

Abstract. The paper describes experimental investigation of the flow and turbulent kinetic energy under the weakly plunging breaking wave in the outer surf zone. Experiments for the present study were carried out on a surf zone model with a constant slope of 1:17 in the vicinity of the wave breaking point. Experimental results show that the kinetic energy is largest under the wave crest and decreases rapidly after the wave crest has passed. Visualization of the flow proved that the velocity profile during backflow phases resembles the steady open channel flow, but during the onflow phases the velocity profile is unlike any other flow situation.

Key words: breaking wave, breaking point, turbulence, kinetic energy field.

1. INTRODUCTION

Experimental investigations of the processes that govern the behaviour of sediments and waves in the surf zone have lasted decades. The first investigations concentrated on the measurements of the free surface of the surf zone during the wave action. The paper [1] paid main attention to the average physical parameters of the wave, whereas the turbulent structure inside the wave was not discussed. From the latter point of view, the real insight into the mechanism of the breaking wave was gained with the introduction of different contact-free measuring techniques like laser Doppler anemometry (LDA) and particle image velocimetry (PIV). Various investigators have used the mentioned systems for measuring velocity fields and turbulent characteristics of the waves. Chang and Liu [2] measured the kinematics of the breaking waves and found that the velocity of the water particles in the wave crest exceeded the wave phase velocity

for 1.7 times. This phenomenon is even more complicated in areas of high entrainment during the breaking process.

With increasing knowledge on the breaking process, mathematicians have proposed several mathematical models to describe it. A common problem is that for accurate representation of the physical phenomenon, the model equations have to contain non-linear terms and therefore there is a necessity to use empirical relations that can only be obtained through experiments. The breaking phenomenon is by nature a non-stationary process, but in most cases, due to the lack of information, the data used is obtained from investigations of similar stationary processes. As the information on non-stationary flow is scarce, there is a great need for further experimental investigations.

The most widely used method for the determination of the velocity field and its turbulent characteristics in breaking waves is LDA. The first publication on LDA measurements in the breaking waves was [3]. Nadaoka and Kondoh [4] defined the inner and outer surf zone, based on the measured characteristics of the breaking waves in these regions. The most comprehensive publications until today are [5–7]. The data from these papers has been used by other authors for comparison and measurement verification. Ting and Kirby [6] found that in case of a plunging breaking wave there is an area of high turbulent intensity in front of the wave crest. This area was found to move perpendicular to the coast line.

The advantage of the PIV method is that it enables one to investigate coherent structures inside the flow. In the first published papers on PIV measurements, Haydon et al. [8] used local averaging to determine average velocity and velocity fluctuations, whereas Chang and Liu [9] used ensemble averaging. The shear stresses on the bottom have been mainly measured using constant temperature anemometer (CTA) techniques. The most comprehensive studies of the surf zone are [10] and [11].

In recent years, numerous experiments have been carried out in the surf zone, not only in the laboratory. The measuring instruments, mainly LDA, mechanical profiling systems, acoustic pressure sensors, video cameras, current meters etc are mounted on tripods. Feddersen and Trowbridge [12] measured the wave generated turbulence in the surf zone and developed a model that is able to reproduce the production and dissipation of turbulence during wave breaking. Trowbridge and Agrawal [13] measured the boundary layer of the wave. Their measurements indicate that there is a reduction in variance and the increase in phase relative to the flow outside the boundary layer. Feddersen and Williams [14] measured the distribution of Reynolds stresses [15] and investigated dissipation near the surf zone. Feddersen et al. [16] investigated drag coefficients, bottom roughness and wave breaking in the near shore area during a two-month campaign.

Another widely used method of investigation of the wave breaking process is mathematical modelling. The mathematical models used can generally be divided into three main groups:
1) classical, averaged wave models;
2) Boussinesq wave models;
3) Navier–Stokes model.

The first two groups of models have been relatively well described in the literature [17]. The increase of computer speed during the last decades has led to more intensive use of models, based on Navier–Stokes equations. This has initiated a separate branch of mathematical modelling, computational fluid dynamics (CFD). CFD allows modelling of different flows with utmost complicated flow kinematics, whereas the result of calculations is relatively accurate. The advantage of CFD is its high precision but the main drawback is the necessity of large computer resources.

The method is based on the Navier–Stokes equations that describe the evolution of the momentum of the water volume. The set of equations consists of the continuity equation

$$\frac{\partial u_i}{\partial x_i} = 0, \tag{1}$$

and equations for the components of the momentum as

$$\rho \frac{\partial u_i}{\partial t} + \rho u_j \frac{\partial u_i}{\partial x_j} = -\frac{\partial p}{\partial x_i} + \frac{\partial}{\partial x_j} \mu \left(\frac{\partial u_i}{\partial x_j} + \frac{\partial u_j}{\partial x_i} \right). \tag{2}$$

Here ρ is the fluid density, u_i and u_j are velocity components, p is pressure, μ is dynamic viscosity, t is time, and x_i and x_j are spatial coordinates.

When turbulent fluctuations can be neglected, relatively good results have been achieved in modelling the processes in the wave boundary layer at low Reynolds numbers using direct numerical simulation method (DNS) [17]. Another method for solving Eqs. (1) and (2) is the large eddies simulation (LES) method [18]. The difference of LES from the DNS method is that in LES the numerical grid has a larger step, and eddies with smaller scale than the grid are modelled using specific parametrizations of subgrid-scale processes. DNS and LES methods require good resolution in all three coordinates and this makes both of them very time-consuming in solving most common engineering problems.

Time-averaged Navier–Stokes equations are most commonly solved using the Reynolds-averaged Navier–Stokes equations (RANS) methods. Here the turbulent velocity u components are treated as a sum of purely averaged $\bar{u}$ and fluctuating u' components

$$u = \bar{u} \pm u' \tag{3}$$

of velocity. Substituting (3) into Eq. (2) leads to the RANS equations:

$$\rho \frac{\partial \bar{u}_i}{\partial t} + \rho \bar{u}_j \frac{\partial \bar{u}_i}{\partial x_j} = -\frac{\partial \bar{p}}{\partial x_i} + \frac{\partial}{\partial x_j} \mu \left(\frac{\partial \bar{u}_i}{\partial x_j} + \frac{\partial \bar{u}_j}{\partial x_i} \right) - \frac{\partial}{\partial x_j} \overline{\rho u'_j u'_i}. \tag{4}$$

In order to close the equations, additional information is needed to determine the Reynolds stresses

$$\tau_{ij} = -\overline{\rho u'_j u'_i}. \tag{5}$$

The analysis of the models that are used for closing the RANS equations [17] shows that the problem can be solved using for kinetic energy or turbulent viscosity coefficients that are obtained from empirical relations for stationary flow.

In order to determine the Reynolds stresses, different viscosity models are used. The most common of them are the $k - \varepsilon$ and the $k - \omega$ models, described in [19,20] (k is turbulent kinetic energy, ε is the dissipation rate of turbulent energy and ω is a variable that determines the scale of the turbulence). With relevant boundary conditions, the RANS and $k - \varepsilon$ models have successfully been used in the description of various complicated turbulent flows [21].

From the above it follows that Reynolds stresses and turbulent viscosity play a major role in closing the governing equations of the models that describe the wave breaking in the surf zone. These parameters can be interpreted in a meaningful way only with a background knowledge from experimental investigations.

Several papers describe experimental investigations of the time-dependent velocity fields in the wave breaking zone [22–25]. These investigations have unfortunately been carried out with different initial conditions, thus making it difficult to generalize the results. At the same time, there are practically no investigations on the variation of the turbulent kinetic energy in time and space in the area around the breaking point. This justifies additional experimental investigations in order to obtain more detailed description of the processes inside the breaking wave and more accurate values for the above mentioned viscosity models.

This paper continues previous investigations on wave breaking [26,27]. It focuses on the kinetic energy distribution around the wave breaking point and discusses the mechanics of the energy transport in the wave. The paper also looks into the mechanism of kinetic energy production from the point of view of local accelerations and decelerations. Presented are measurement results, obtained during the wave period, i.e. two-dimensional time-dependent fluctuating turbulent velocity components inside the breaking wave. These results allow more accurate description of the quantities used for closing Eqs. (4) and (5), and the calculation of time-dependent turbulent kinetic energy and eddy viscosity. The results have been obtained in the vicinity of the wave breaking point and thus give additional insight into the processes associated with wave breaking.

2. EXPERIMENTAL SET-UP

The aim of the experiments is the determination of the non-stationary flow field parameters at the wave breaking point and around its immediate vicinity. The experiments were performed in the wave flume of the Tallinn University of Technology to study the variation of the two-dimensional flow fields during the breaking process perpendicular to the shoreline. For this purpose regular waves were generated in the wave flume. Vertical and horizontal velocity components

under the weakly plunging breaking wave were measured with LDA. As a result of measurements in 29 sections at 1852 points along the surf zone slope perpendicular to the shoreline, the time-dependent two-dimensional flow fields were measured.

2.1. Description of the experimental set-up

The wave flume used was 0.6 m wide, 0.6 m deep and 22 m long (Fig. 1). The transparent walls of the flume were made of glass and the bottom was made of vinyl plates. Waves were generated in the section of constant depth of the flume, which was 12.45 m long. The average water depth in the constant depth section was kept equal to 0.3 m. Regular waves were generated with the flap-type wave generator with a constant wave period $T = 2.03$ s. The parameters, describing the breaking wave, are listed in Table 1. In Table 1, h_b is the water depth at the breaking point including the change of water level due to wave set-up, d_b is the still water depth at the breaking point, H_0 is the deep water wave height, L_0 is the deep water wavelength and H_b is the wave height at the breaking point. Before the measurement procedures were initiated, the waves were let to run for 30 min to allow to decrease the reflection-caused second harmonic waves and to establish an adequate wave set-up.

The measurement section was chosen so that it incorporated also the breaking point. Wave breaking was investigated on a surf zone model with constant slope of $1:17$. The velocity field inside breaking waves was measured with two-component argon-ion LDA with an output power of 1.3 W. Forward scatter mode was used throughout the experiments.
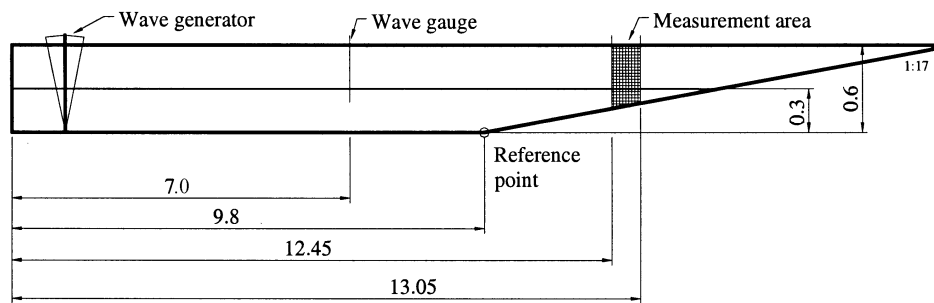

Fig. 1. Wave flume, dimensions in m.

Table 1. Parameters, describing the weak plunging breaker

T, s	h_b, m	d_b, m	x_b, m	H_0, m	H_0/L_0	H_b, m	H_b/d_b
2.0	0.106	0.111	2.90	0.072	0.012	0.118	1.06

As the LDA system allows measurement only at one point, the measurements were repeated over the vertical for all 29 sections. The measuring net had a variable step. Distance between the measuring sections was 1 cm before the breaking point and 3 cm after it. The measuring step along the vertical was 1 mm in the near-bed zone, 3 mm in the intermediate zone and 2 mm in the zone, affected directly by wave action. The lowest point was 0.05 mm above the bottom.

Wave parameters were kept constant throughout the experiments. The wave similarity was controlled with a synchronizing mechanism and analysed with methods described below. The working principle of the synchronizing mechanism is described in [27]. The wave parameters and location of the measuring points are given in Table 2.

Table 2. Location of measuring points and corresponding wave parameters

Cross-section No.	No. of measuring points on the vertical	Distance from the point A x, m	Still water depth d, m	Water depth with wave set-up h, m	Wave celerity C, m/s
29	47	3.21	0.089	0.089	0.933
28	47	3.18	0.091	0.091	0.944
27	48	3.15	0.093	0.093	0.955
26	50	3.12	0.095	0.095	0.964
25	51	3.09	0.098	0.097	0.975
24	51	3.06	0.100	0.099	0.983
23	53	3.03	0.102	0.100	0.990
22	54	3.00	0.104	0.101	0.997
21	55	2.97	0.106	0.102	1.001
20	58	2.94	0.108	0.104	1.010
19	58	2.91	0.110	0.104	1.012
18	61	2.82	0.117	0.114	1.059
17	61	2.81	0.118	0.115	1.064
16	62	2.80	0.118	0.116	1.069
15	62	2.79	0.119	0.117	1.071
14	65	2.78	0.120	0.118	1.077
13	65	2.77	0.120	0.119	1.079
12	64	2.76	0.121	0.119	1.082
11	66	2.75	0.122	0.120	1.086
10	63	2.74	0.123	0.121	1.090
9	67	2.73	0.123	0.121	1.091
8	69	2.72	0.124	0.122	1.094
7	69	2.71	0.125	0.123	1.098
6	70	2.70	0.125	0.124	1.101
5	70	2.69	0.126	0.124	1.104
4	70	2.68	0.127	0.125	1.108
3	69	2.67	0.128	0.126	1.111
2	76	2.66	0.128	0.127	1.115
1	151	2.65	0.129	0.127	1.117

2.2. Procedures

Experimental data from six channels were recorded simultaneously. The channels were connected to the computer through an analogue–digital converter. During experimental runs, horizontal and vertical velocity components, the corresponding signal dropouts, water level variation and signals from the synchronizing mechanism were saved. In order to achieve reliable results during ensemble averaging, data was collected for 151 wave periods ($T = 2.03\,\mathrm{s}$). The sampling frequency was 1000 Hz, thus for each measuring location $6 \times 306\,530$ data points were recorded. Total number of the measuring points was 1852.

In order to filter the experimental results, dropout signals were used. By measurements with the LDA system, dropouts occur when the measuring volume is not formed by the laser beams or the beam is blocked by a solid object, for instance by a sediment particle. Thus the dropout signal shows if the measured value is true or not.

The use of the signal from the synchronizing mechanism is mostly necessary for the synchronization of the data. The synchronizing mechanism was made of two stainless steel wires. The existence of electric conductivity between the wires showed whether the synchronizing mechanism was in water or not. If the synchronizing mechanism was in water, the signal value was 1 and if out of water, then 0. The location of the synchronizing mechanism was kept constant during the whole experiment. Experimental runs were started when the value of the signal had been 1 for at least 50 ms to avoid false information from possible water sprays.

A common problem with the experiments in the wave flume is how to achieve the generation of waves with a constant period. The shortcoming of the wave flume is usually the generation of reflected waves between the wave generator and the surf zone model. The easiest way to deal with the problem is to perform measurements before the reflected waves occur. In the present case it was impossible, as the number of wave periods in the experimental run was 151. For this reason the reflected wave was taken as part of the wave. In the following we investigate the behaviour of the reflected wave; 1250 wave periods were measured after the start-up of the generator. The result is depicted in Fig. 2. It can be seen from the figure that after the initial stabilization the wave period is approximately 2.02 s. After wave number 500 the wave period stabilizes at 2.03 s. This new wave period stays virtually unchanged for the rest of the working time of the generator. The mean wave period is achieved at wave 1680, i.e. 28 min after starting the wave generator. For this reason, waves were always let run at least 30 min before starting the measurements.

The turbulent flow velocity can be described as the sum of the averaged velocity and the fluctuating component:

$$u_i(t) = \langle u_i(t) \rangle + u_i'(t), \tag{6}$$

where $u_i(t) = (u(t), v(t), w(t))$ is the measured velocity, $\langle u_i(t) \rangle$ is the averaged velocity and $u_i'(t)$ reflects turbulent fluctuations. As mentioned in the introduc-

48
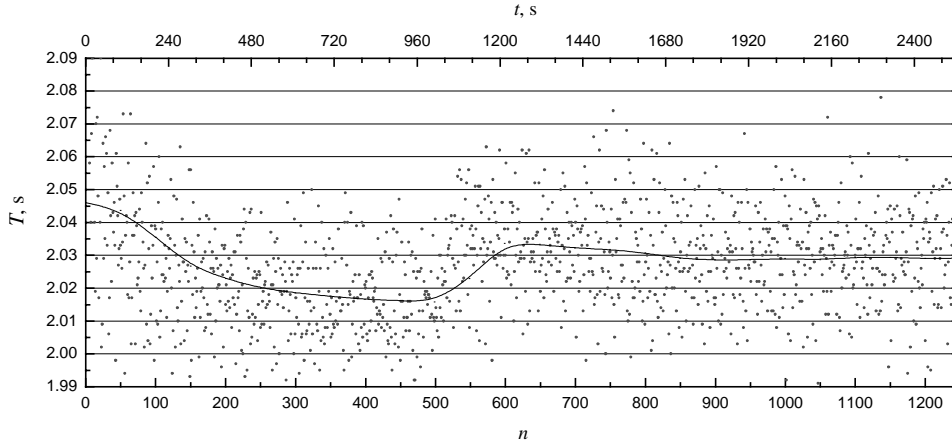
Fig. 2. Stabilization of the wave periods after the start of the wave generator; n – number of the wave.

tion, the most common way of defining the averaged velocity is the ensemble (phase) averaging. The ensemble-averaged velocity is calculated as

$$\langle u_i(t) \rangle = \frac{1}{N} \sum_{k=0}^{N-1} u_i(t+kT), \quad 0 \le t \le T, \tag{7}$$

where N is the number of waves. This method, however, requires very precise repetitions of the phenomena under investigation. Although the wave period stabilized in 30 min, this did not mean that all waves that entered the measuring section had the same period. As seen in Fig. 2, wave periods fluctuate to some extent and have a distribution as shown in Fig. 3 for 12 consequent experimental runs (1812 waves). The vertical axis gives the number of occurrences and the horizontal axes shows the wave period. The deviation from the mean period is only about ±0.03 s that makes only about 1.5% of the whole wave period. So the waves can be considered to be regular.

Since all waves did not have the same period, the usual way of ensemble-averaging was not applicable. Instead, a modified ensemble-averaging method was derived.

The first step is to find the average wave period (2.03 s) and also all individual wave periods of all waves during the experimental run. Then all waves are scaled so that they have the same length. For instance, if the period is longer ($n = 2050$ points, sampling frequency is 1000 Hz, meaning that 2050 points correspond to the wave period 2.05 s), the necessary amount of points are evenly removed from the period so that the period is exactly 2030 points. If the period is shorter than the average, the necessary amount of points is evenly added to the period. All added points are given a dropout value and they are disregarded from the analysis. All very short and long period waves (by 30 points larger or smaller

49
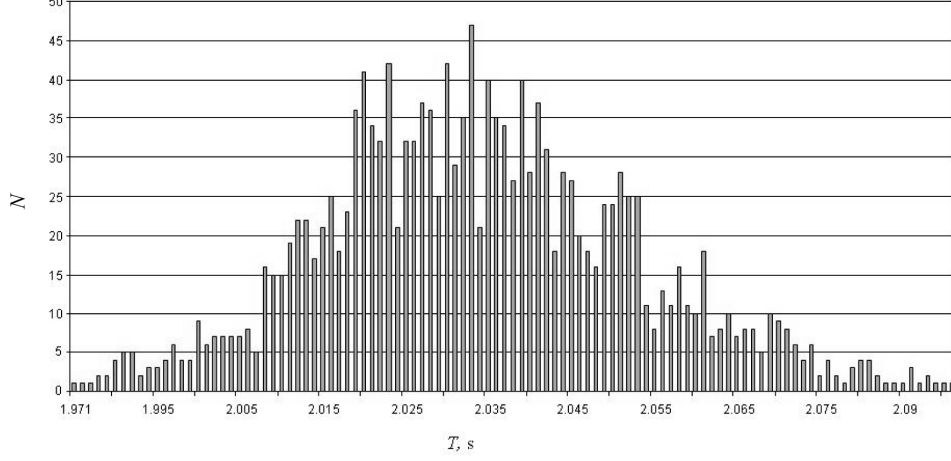
Fig. 3. Spectrum of wave periods for 12 consequent experimental runs.

than the average value) are removed from the analysis. Finally, the ensemble-average velocity is found from the equation

$$\langle u_i(t) \rangle = \begin{cases} \dfrac{1}{N} \displaystyle\sum_{k=0}^{N-1} u_i^*(t + kT_m) D_i(t + kT_m), & N_D \geq 10, \\ 0, & N_D < 10, \end{cases} \quad 0 \leq t \leq T_m, \quad (8)$$

where $u_i^*(t)$ is the time-scaled velocity, T_m is the mean wave period, $D_i(t)$ is the dropout signal and N_D is the actual number of summed values (i.e. points with $D(t) = 1$). If the ensemble-averaged value is 0, then the measured data is not reliable. A similar method has also been used in [24].

According to Eq. (6), the turbulent fluctuations can be calculated as

$$u_i'(t) = u_i(t) - \langle u_i(t) \rangle. \quad (9)$$

The classical ensemble-averaging method calculates the turbulent fluctuations as

$$u_i'(t) = \frac{1}{N} \sqrt{\sum_{k=0}^{N-1} (u_i(t + kT) - \langle u_i(t) \rangle)^2}, \quad 0 \leq t \leq T. \quad (10)$$

Similarly to the averaged velocity, the values of the root-mean square of turbulent fluctuations were found using modified ensemble-averaging

$$\langle u_i(t) \rangle = \begin{cases} \dfrac{1}{N} \sqrt{\displaystyle\sum_{k=0}^{N-1} (u_i^*(t + kT_m) - \langle u_i(t) \rangle)^2 \cdot D_i(t + kT_m)}, & N_D \geq 10, \\ 0, & N_D < 10, \end{cases} \quad 0 \leq t \leq T_m. \quad (11)$$

50

As the LDA system used measured only two components of the velocity, the turbulent kinetic energy was calculated using the method proposed in [28]

$$k(t) = \frac{1.33}{2}(u'^2(t) + v'^2(t)).$$ (12)

2.3. Data processing

The beginning of the coordinate axes is located at the average water level at the beginning of the declined part of the bottom of the flume (Fig. 4). The measured data is presented in non-dimensional form: the horizontal coordinate x_1 is defined as

$$x_1 = \frac{x - x_b}{h_b}.$$ (13)

At the breaking point $x_1 = 0$, $x_1 > 0$ if $x > x_b$ and $x_1 < 0$ if $x < x_b$.
The dimensionless coordinate y_1 is defined as

$$y_1 = \frac{y - \eta}{h},$$ (14)

where η is instantaneous surface elevation. The surface elevation in case of breaking waves is expressed as

$$\eta_1 = \frac{\eta - \bar{\eta}}{h},$$ (15)

where $\bar{\eta}$ is the ensemble-averaged surface elevation.
The normalization of velocity components and of the turbulent kinetic energy is carried out using the local wave phase velocity C:

$$C = \sqrt{gh},$$ (16)
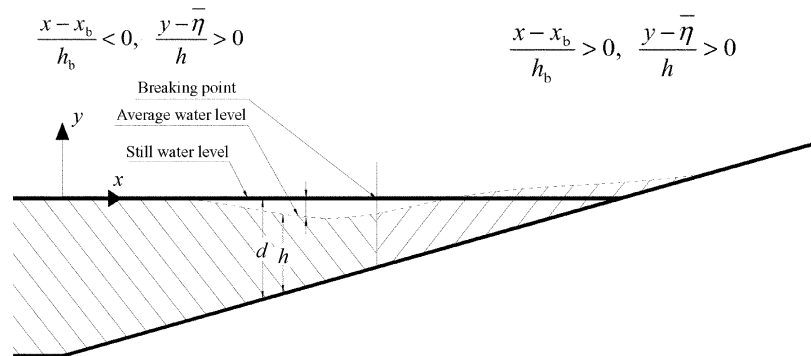
where g is the acceleration due to gravity.

Fig. 4. Definition of flow parameters.

51

3. EXPERIMENTAL RESULTS

3.1. Time series

Figure 5 shows the surface elevation, ensemble-averaged horizontal and vertical velocity components and turbulent kinetic energy in different cross-sections. The measurements were performed in 29 cross-sections, from which three are chosen to be depicted in the present article: $(x - x_b)/h_b = -2.36$, $(x - x_b)/h_b = 0.09$ and $(x - x_b)/h_b = 2.17$. These cross-sections characterize the situation before breaking, during the initial breaking process and after the breaking has occurred.

The surface elevation is depicted in Figs. 5A to 5C. It can be seen that the surface elevation in different cross-sections is not constant. In comparison with the inner surf zone measurements in [7] and [29], where the value $(\eta - \bar{\eta})/h$ was almost constant, the surface elevation in the outer surf zone changes considerably, especially in the region of initial breaking. Here the maximum surface elevation is equal to the average water depth and minimum surface elevation is 1.5% of the average water depth. This result agrees with [6]. The ratio of the wave height to the water depth H/h is 1.13 that is remarkably larger than the usual value (about 0.8) of the wave breaking parameter.

Figures 5D to 5F show the variation of the ensemble-averaged horizontal velocity component during one wave period. The horizontal velocity component follows the variation of surface elevation. There is a secondary crest after the velocity maximum. This secondary wave is generated by the backflow of water from the shoreline. Similar secondary waves have been described also in [6].

Before the wave breaks, the maximum of the horizontal component reaches about $0.4C$ in all cross-sections. After the crest, this similarity between the cross-sections disappears. The non-dimensional horizontal velocity varies between $0.15C$ and $0.8C$.

Close to the still water level, the horizontal velocity component is zero. This means that at this location no reliable data is available. In the present case it means that the measuring volume was not formed, due to the fact that the laser beams were out of the water in the wave trough. In most of the studies this data is not presented.

Figures 5G to 5I show the variation of the ensemble-averaged vertical velocity component. The maximum value of the vertical velocity is always reached during the maximum acceleration of the horizontal velocity. The maximum of the vertical component moves along the wave crest, in front of it. This is the location, where backflow from the previous wave and the onshore movement of the new wave meet and where water has nowhere else to go than upwards. The maximum acceleration of the horizontal velocity can be explained by the sudden reversal of the flow.

From the experimental data it can be concluded that during the maximum deceleration of the horizontal velocity component the vertical velocity in the upper layers of the water column achieves its minimum value. This result
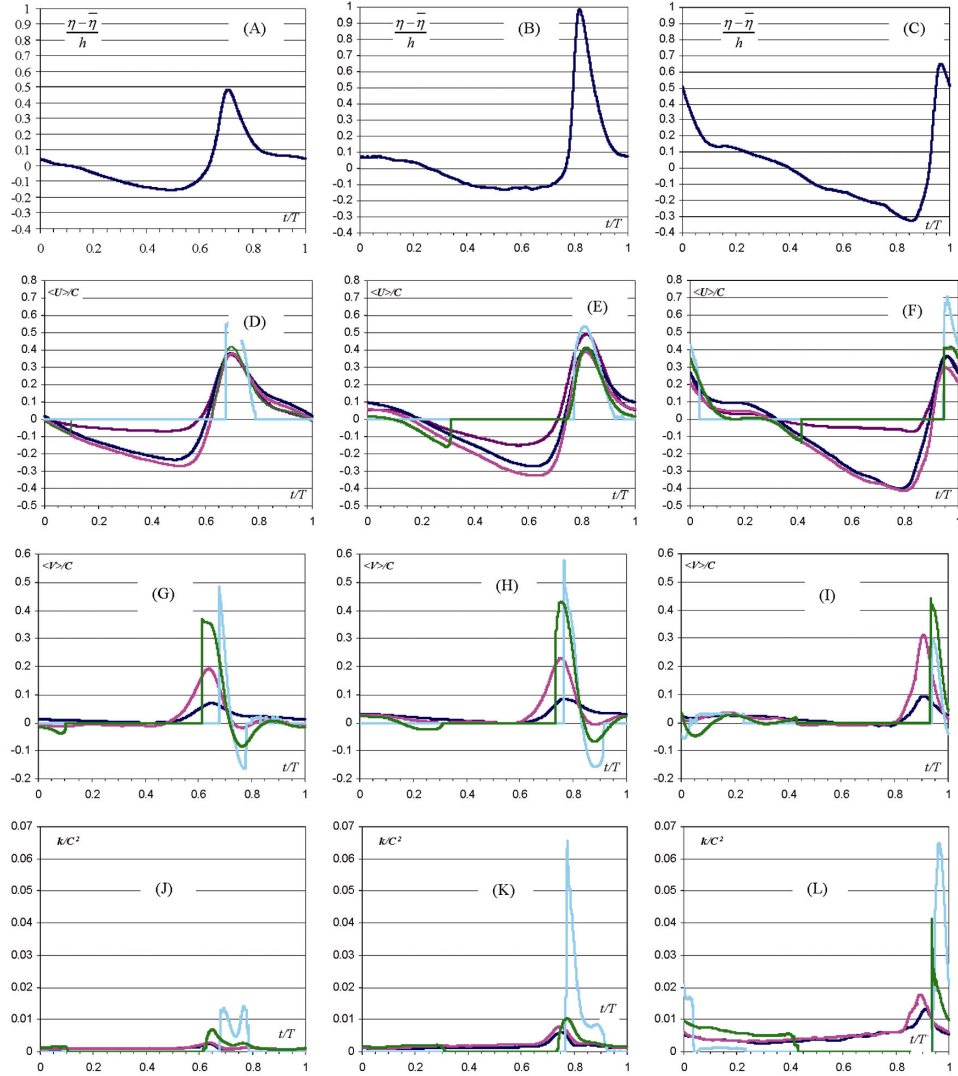
Fig. 5. Surface elevation (A–C), horizontal velocity component (D–F), vertical velocity component (G–I) and turbulent kinetic energy (J–L) in cross-sections $(x - x_b)/h_b = -2.36$ (left column), $(x - x_b)/h_b = 0.09$ (centre column) and $(x - x_b)/h_b = 2.17$ (right column) at the heights:

—— $(y - \bar{\eta})/h = -0.99$, —— $(y - \bar{\eta})/h = -0.89$, —— $(y - \bar{\eta})/h = -0.54$,

—— $(y - \bar{\eta})/h = -0.17$, —— $(y - \bar{\eta})/h = 0.18$.
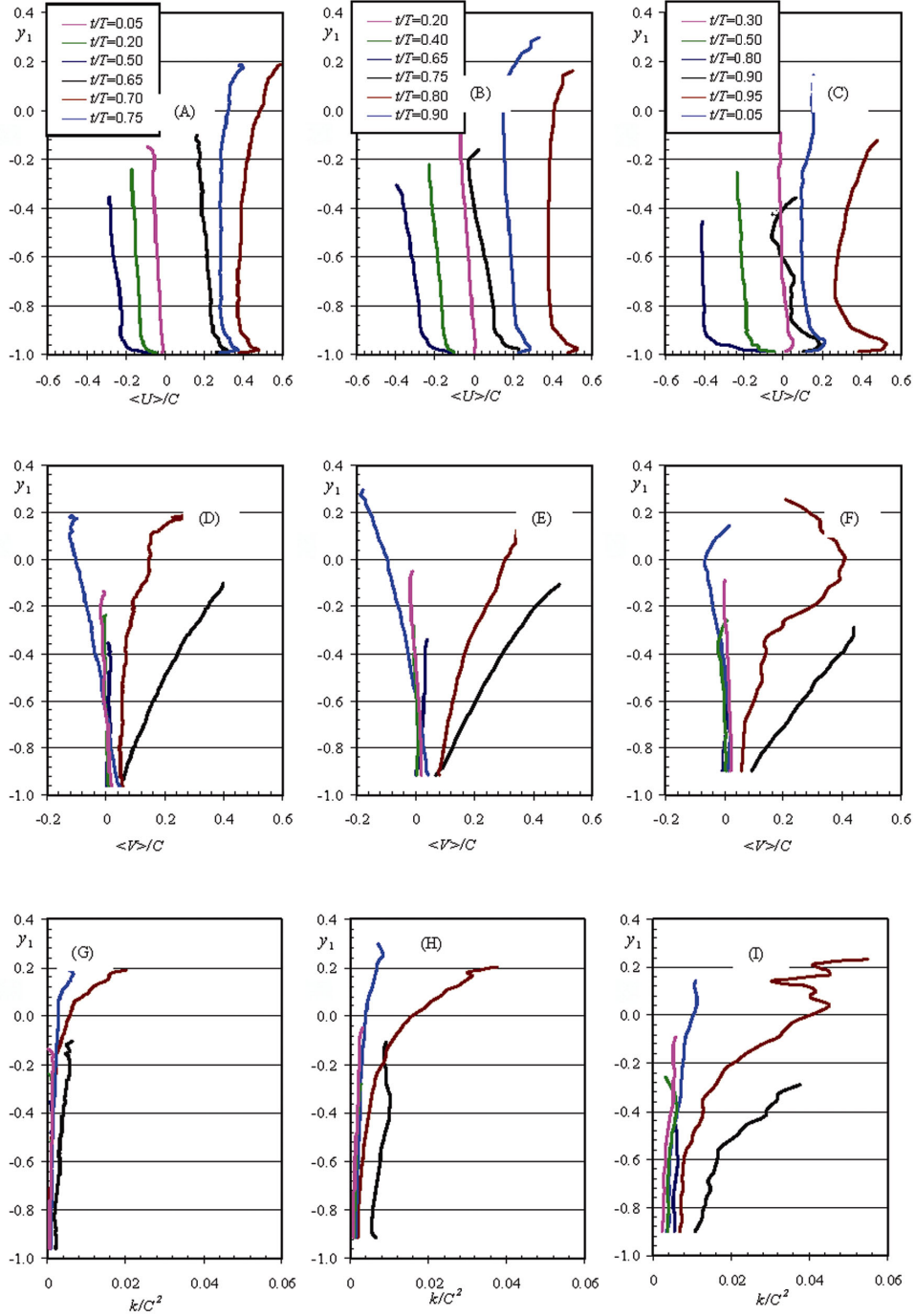
Fig. 6. Ensemble-averaged horizontal (A–C) and vertical (D–F) velocity and turbulent kinetic energy (G–H) profiles; left column: $(x - x_b)/h_b = -2.36$; middle column: $(x - x_b)/h_b = 0.09$; right column: $(x - x_b)/h_b = 2.17$. ,

54

supports the Marker and Cell (MAC) method [30], which has been used to model the processes on the coastline. In MAC method all computational elements are given as markers, which move according to the calculated velocity field.

The maximum value of the vertical component of velocity in the intermediate layers of the water column is about $0.2C$ before the breaking point, which is in good agreement with earlier investigations [6]. Near the still water level the value is about $0.5C$. After the breaking point, during the backflow phase of the wave, the value of the vertical velocity component in all layers approaches zero.

The time series of the turbulent kinetic energy are presented in Figs. 5J to 5L. The kinetic energy has two local peaks. They correspond to local extremes of the vertical velocity component and also to the maximums of the acceleration and deceleration of the horizontal velocity component. While before breaking the energy levels before and after the wave crest are approximately equal, then as the breaking process develops, the kinetic energy precedes the wave crest. This is one of the major differences between spilling and plunging breakers. According to [19], the energy maximum inside the spilling breaker moves behind the wave crest.

Before breaking, the level of turbulent kinetic energy is low. The energy is generated only in the upper layers of the water column, reaching there the level of about $0.015C^2$ under the wave crest. When breaking is initiated, the energy level grows considerably and reaches also the bottom layer. This suggests that the wave front has plunged into the wave crest in front of it. After the breaking point the maximum measured kinetic energy was about $0.65C^2$. It is also interesting to follow the development of the levels of turbulent kinetic energy along the surf zone model. The energy before the wave crest at $(x - x_b)/h_b = -2.36$ and immediately after breaking at $(x - x_b)/h_b = 0.09$ have a value less than about $0.001C^2$. In the third cross-section, at $(x - x_b)/h_b = 2.17$, the level of turbulent kinetic energy before the wave crest has increased nearly by 5 times. In this cross-section large-scale eddies have reached the bottom and the mixing processes have carried the turbulent kinetic energy all over the water column.

3.2. Ensemble-averaged profiles

Figure 6 depicts vertical distributions of the horizontal and vertical ensemble-averaged velocities and turbulent kinetic energy at different moments. Similarly to Fig. 5, the profiles under investigation are located at $(x - x_b)/h_b = -2.36$, $(x - x_b)/h_b = 0.09$ and $(x - x_b)/h_b = 2.17$.

Figures 6A to 6C depict the variation of the horizontal velocity component at different time moments in the three above mentioned profiles. There are two types of lines in the figures. The lines coloured pink, green and dark blue represent the backflow from the beach; lines coloured black, brown and light blue represent the onflow towards the beach. The flow profiles during backflow resemble the classical steady flow profiles in open channels. During onflow towards the beach, the velocity profiles are remarkably different from the steady open channel flow. The measurements show that during the onflow, the horizontal velocity of the

water particles is larger in the near-bed zone and in the layers close to the water surface than in the intermediate layers. This can be explained with the backflow of water that decelerates the water particles in the intermediate zone to such a level that an almost homogeneous flow pattern is formed in the given zone. The Boussinesq type wave models for the beach make the same assumption [31].

The ensemble-averaged distributions of the vertical velocity component are shown in Figs. 6D to 6F. Similarly to the horizontal velocity component, the backflow values of the vertical velocity component resemble open channel flow. During backflow the value is approximately zero. During the wave phases, when the flow is directed towards the shore, the vertical velocity changes linearly from zero at the bottom to about $0.4C$ above the still water level. This means that under the wave crest water is "pulled" into the crest during wave propagation and the shoaling process (brown and black lines). The light blue line represents the phase of the wave when water is intensively flowing out from the wave crest. This results in the increase of the negative (directed towards the bottom) flow velocity. This phenomenon is especially pronounced in the profiles near the breaking point at $(x - x_\mathrm{b})/h_\mathrm{b} = 0.09,$ where the velocity reaches about $0.2C$. At $(x - x_\mathrm{b})/h_\mathrm{b} = 2.17$ this value is more than twice smaller. This suggests that the wave has entered the area of wave setup.

Figures 6G to 6I show the distribution of turbulent kinetic energy. It can be noticed that before breaking (G) the level of kinetic energy is low. There is only a slight increase of turbulent kinetic energy in the wave crest. The next figures (H and I) show how the kinetic energy diffuses towards the bottom layers. This phenomenon becomes first evident under the crest and as the wave progresses also during the backflow phases.

3.3. Variation of the turbulent kinetic energy across the surf zone

In the present study the measured profiles of the turbulent kinetic energy are close enough to give a qualitative picture of its variation over the whole measured area. As mentioned before, the horizontal step between the profiles was 10 mm before the breaking point and 30 mm after it.

Figure 7 gives the time-averaged variation of the turbulent kinetic energy across the surf zone at different non-dimesional heights above the bottom. These values have been obtained during the analysis of turbulent fluctuations using Eq. (12). The analysis of measured data shows that the level of turbulent kinetic energy is increased as we approach the shore. Figure 7 shows clearly that after the wave has plunged into the trough, the level of turbulent kinetic energy increases, especially above the still water level.

The level of the kinetic energy and also turbulence intensity are low until the wave crest plunges. The plunging point is probably characterized by especially high values of turbulence intensity, but due to the high level of air entrainment it is impossible to measure it using LDA techniques. It has been suggested that the intensity of turbulence there is more that ten times higher than in other parts of the wave.

56
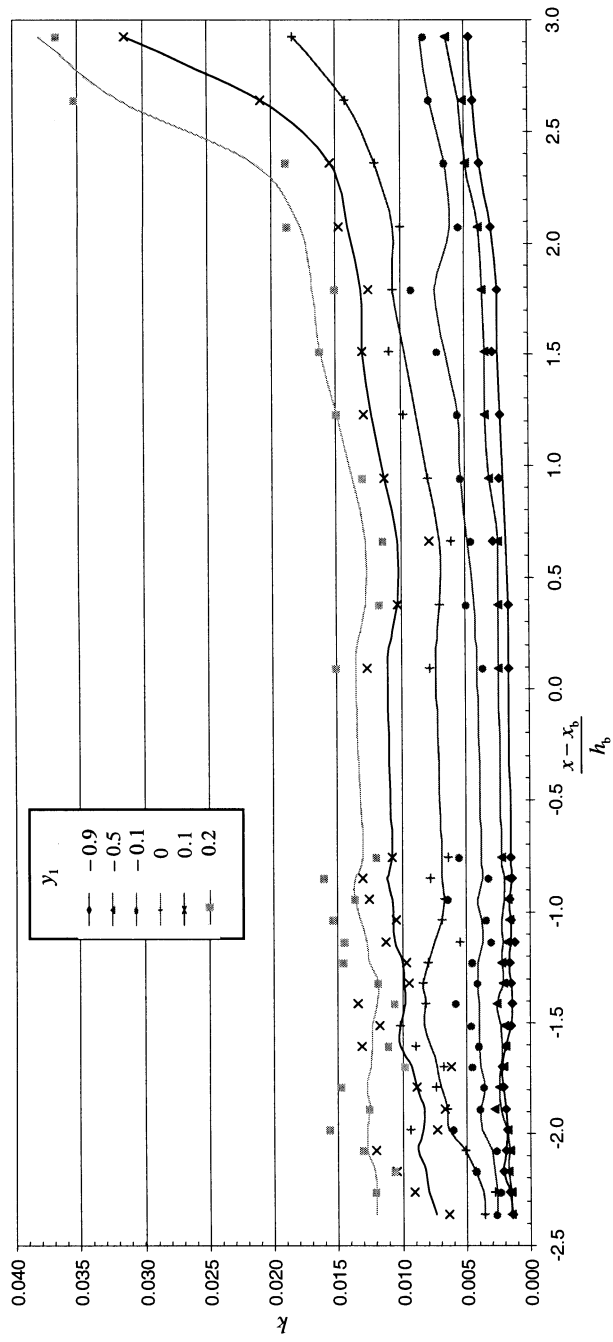
Fig. 7. Time-averaged variation of turbulent kinetic energy perpendicular to the coastline at different heights above the bottom.

57

The development of PIV methods and computer graphics has led to the usage of field graphs in the description of breaking waves [32,33]. The advantage of field graphs in comparison to conventional methods is that it enables one to follow the qualitative nature of the breaking process. The field graphs in the case of LDA measurements are usually not presented as there is not sufficiently data. In the case of the present experimental run, the measured data had a sufficiently high spatial resolution to make it possible to present field graphs.

3.4. Velocity vector and turbulent kinetic energy fields around the breaking point

Figures 8 to 13 present velocity vectors and turbulent kinetic energy fields for the measured area under the breaking wave. As the vertical resolution of measurements is very high, only every third point is depicted. The figures show also the still water level, instantaneous surface profile and the wave flume bottom. In the white area between the surface profile and the coloured kinetic energy plots the measurements did not give reliable data due to high air entrainment or lack of laser beams in the water. In order to get a better understanding of the processes involved, the length scale of the vectors in all the figures is kept the same. Due to this, very low velocities are represented by an arrow that shows the direction of the flow.

At $t/T = 0.4$ and 0.5 there is backflow all over the measuring section. Here the flow resembles very much analogues flows in open channels. The same could be concluded from the flow profiles in Fig. 6. The first signs of the arrival of the wave crest appear at $t/T = 0.6$ when the surface starts to elevate and the magnitude of the vertical component of velocity becomes comparable with the horizontal component. At $t/T = 0.7$, the wave crest has entered the measuring section. At this time moment the process of meeting the flows towards and from the shore can easily be followed. This process eventually results in the increase of the water column in the wave and the breaking of the wave. There is always an area in front of the wave crest, where water particles move towards the surface perpendicular to the wave movement direction. This phenomenon is caused by the collision of the water masses moving towards each other. This movement is more intense near the still water level. Figures 12 and 13 show that the movement of water particles in the upper layers of the water column behind the wave crest is directed slightly downwards, showing that the lowering water surface presses water particles down.

Figure 5 shows that at time moments when vertical movement of water particles precedes the crest, the horizontal component of velocity is zero and it changes the sign.

The obtained velocity fields lead to the conclusion that there is one large-scale vortice under the breaking wave with its vertical dimension approximately equal to the water depth and the horizontal dimension approximately equal to the wave amplitude.
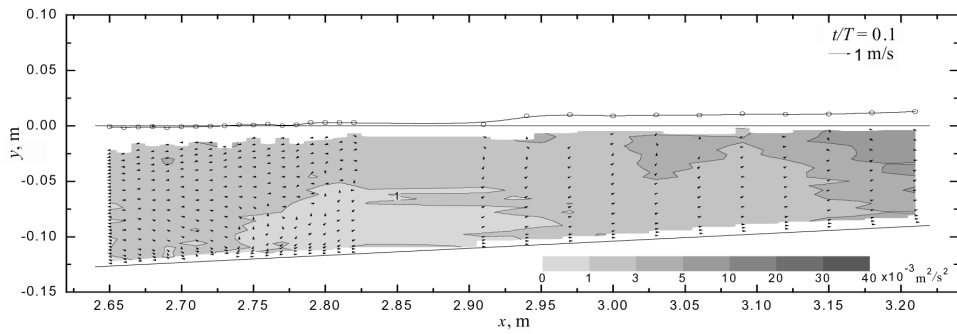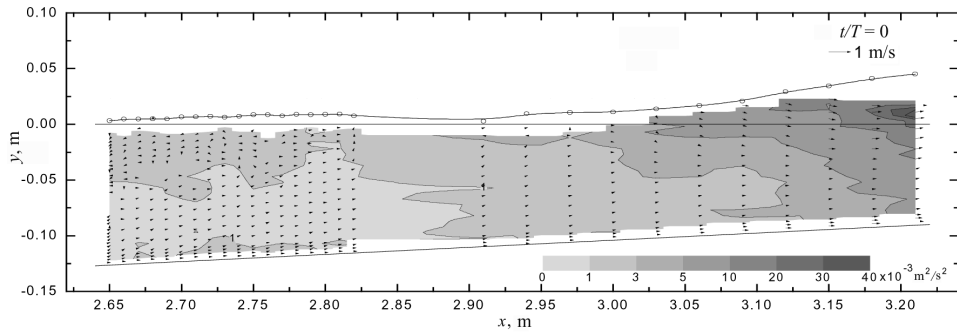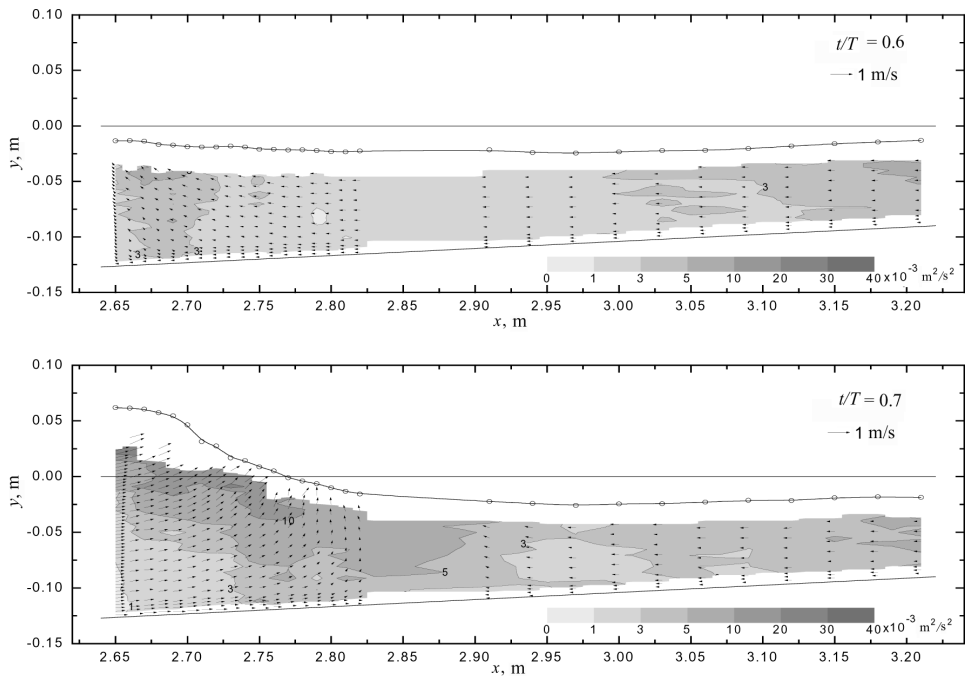
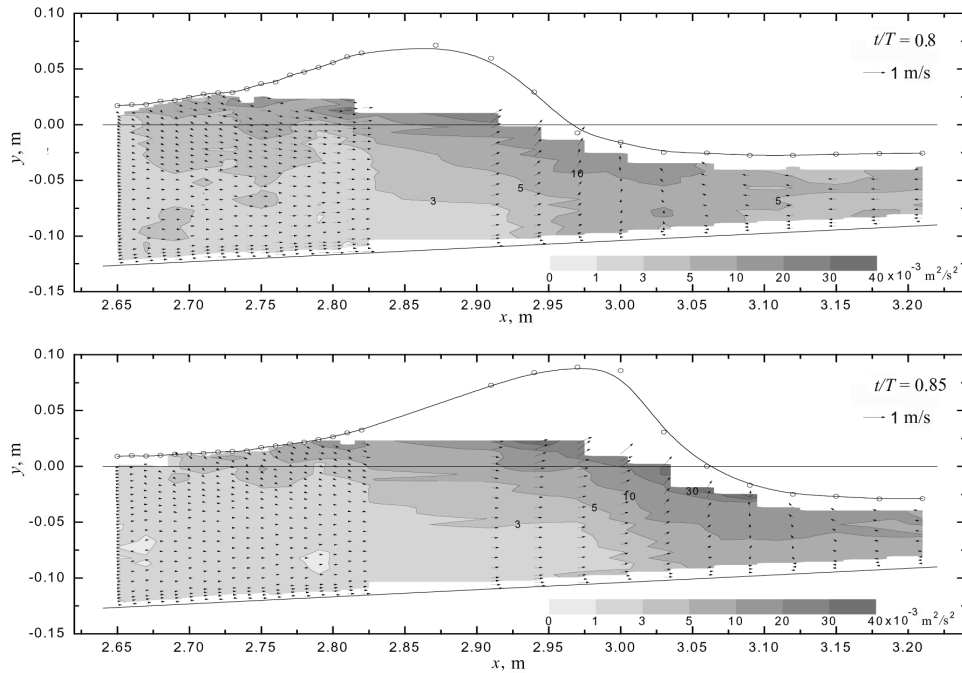**Fig. 8.** Turbulent kinetic energy and velocity field at *t/T* = 0.0 and 0.1.
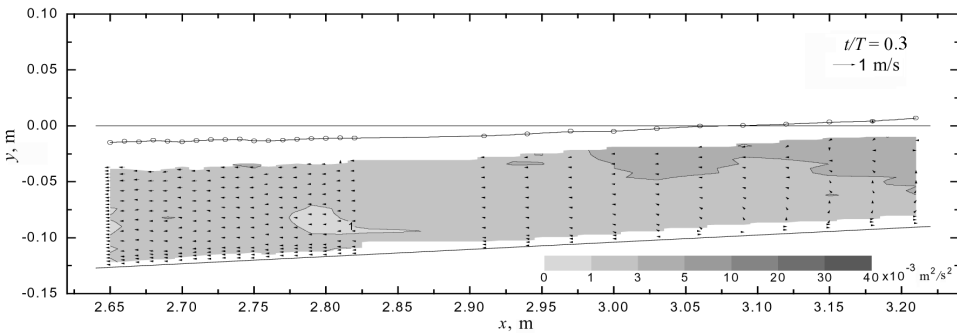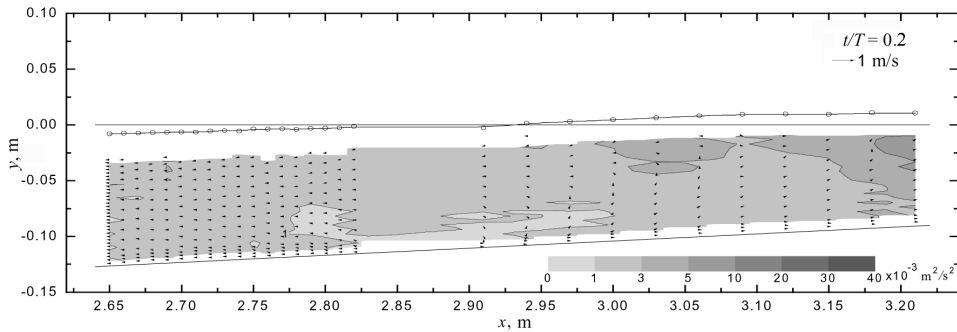
Fig. 9. Turbulent kinetic energy and velocity field at *t/T* = 0.2 and 0.3.
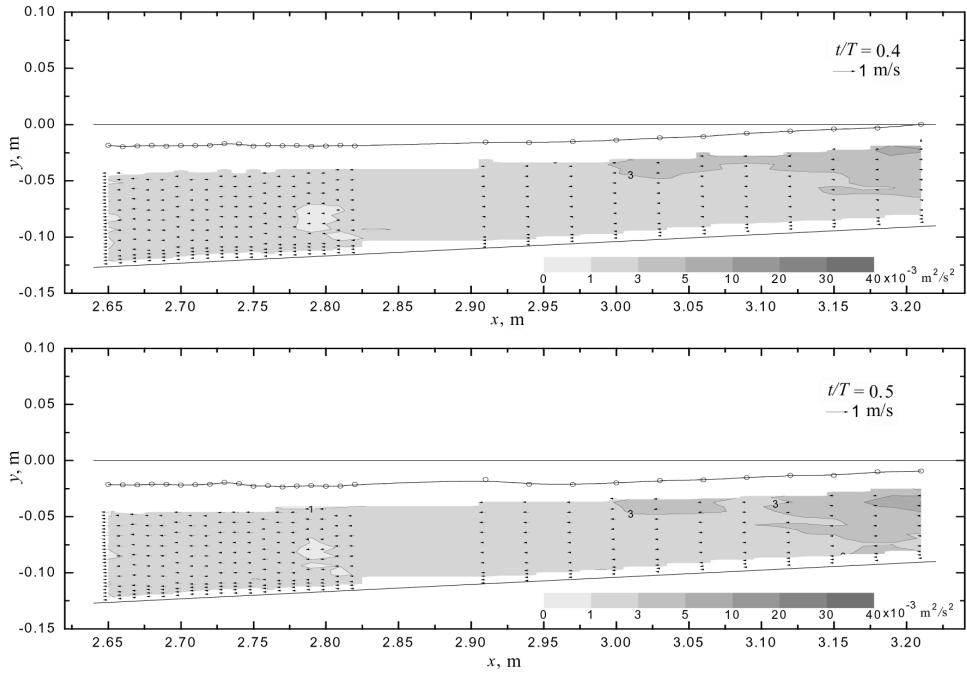
Fig. 10. Turbulent kinetic energy and velocity field at $t/T = 0.4$ and 0.5.

Fig. 11. Turbulent kinetic energy and velocity field at $t/T = 0.6$ and 0.7.

60
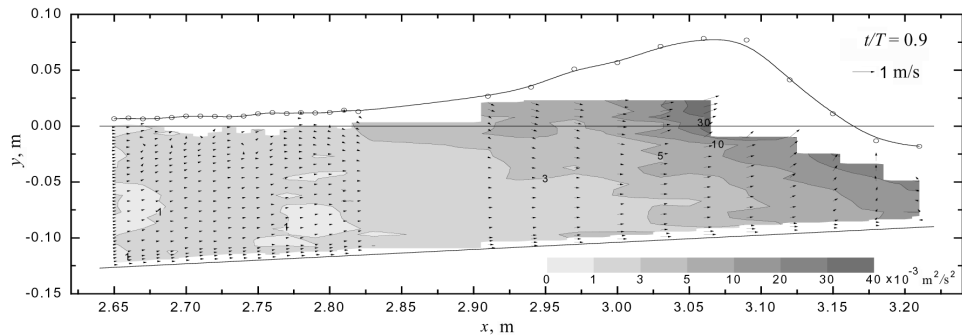
Fig. 12. Turbulent kinetic energy and velocity field at $t/T = 0.8$ and 0.85.

Fig. 13. Turbulent kinetic energy and velocity field at $t/T = 0.9$.

Besides the velocity vector fields, Figs. 8 to 13 present also turbulent kinetic energy fields in the breaking wave. In order to show both very low and high values of turbulent kinetic energy, a non-linear scale has been used. To the knowledge of the authors, similar graphs have not been published earlier.

Higher values of the turbulent kinetic energy are concentrated in the area under and before the wave crest (cf $t/T = 0.7$ to 0.9). The shoreward moving wave crest generates more and more energy that through dispersion spreads towards the bottom. At $t/T = 0.7$, when the crest is situated before the breaking point ($x = 2.90$ m), the turbulence, generated in the wave crest, starts spreading downwards. It reaches the bottom at $t/T = 0.9$.

The area with the largest values of turbulent kinetic energy is located at the wave crest. Figure 5 shows that the generation of the turbulent energy takes place in front of the crest, where the acceleration of the horizontal velocity component is the largest. This fact shows that energy is drawn from the generation zone and carried along with the wave.

The second area with a relatively high turbulent energy level is located behind the wave crest. Figure 5 shows that in this area the horizontal velocity is decelerating. The increase of turbulent fluctuations and hence also of turbulent kinetic energy has been noticed also by other authors [34]. The third area of generation of turbulence is the bottom boundary layer. Since during the present experimental run the smooth bottom was used, the increase of turbulent energy due to the bottom boundary layer is not large. It has been shown that the generation of turbulence by the boundary layer even in case of rough bottoms is neglible in comparison with the generation from the wave crest. Turbulent energy is therefore concentrated in the wave crest and in the rest of the wave there is practically no turbulent energy [6]. Turbulence is generated in front of the wave crest, drawn into it and carried on by it. Most of the turbulent energy dissipates behind the wave and during the breaking process. The same conclusion was also made in [19].

4. CONCLUSIONS

The present study concentrated on the behaviour of the plunging breaking wave in the outer surf zone. Experiments were carried out in the wave flume with a smooth bottom. The surf zone model had a constant slope of $1:17$. Water particle velocities were measured with LDA technology.

During wave phases, when flow is directed away from the shoreline, the ensemble-averaged profiles of the horizontal velocity component resemble the profiles of the steady open channel flow. During the phases, when flow is directed towards the shore, the horizontal velocity of the water particles is larger in the near-bed zone and in the layers close to the water surface than in the intermediate layers.

The ensemble-averaged vertical velocity component gains its maximum value simultaneously with the maximum acceleration of the horizontal velocity component. In the upper layers of the water column, behind the wave crest the vertical component of velocity is always negative, and during backflow phases the value is close to zero.

As a result of the experimental investigations, two-dimensional flow and energy fields have been calculated. These allow to make the following conclusions.
– The turbulent kinetic energy has two local maximums that correspond to the extreme values of the vertical and horizontal accelerations.
– Before the breaking point, the time-averaged turbulent kinetic energy is practically constant. It starts increasing from the breaking point and has a sudden increase immediately before the crest plunges into the preceding trough.

– After the breaking point, the maximum value of the turbulent energy is located at the crest, from where it spreads all over the water column. This is different from the spilling breaking wave, where the turbulent fluctuations do not reach the bottom.
– There is always an area with water particles with purely vertical velocity, travelling in front of the wave crest. This phenomenon is more evident in the area immediately under the stillwater level.
– The turbulent kinetic energy, generated in the crest during the breaking process, dissipates immediately after the wave has passed.

ACKNOWLEDGEMENT

REFERENCES

1. Svendsen, I. A. and Hansen, J. B. Determination up to breaking of periodic waves on a beach. In *Proc. 16th Coastal Engineering Conference*. Hamburg, 1976, 477–496.
2. Chang, K.-A. and Liu, P. L.-F. Experimental investigation of turbulence generated by breaking waves in water of intermediate depth. *Phys. Fluids*, 1999, **11**, 3339–3400.
3. Stieve, M. J. F. Velocity and pressure field of spilling breaker. In *Proc. 17th Coastal Engineering Conference*. Sydney, 1980, 574–566.
4. Nadaoka, K. and Kondoh, T. Laboratory measurements of velocity field in the surf zone by LDV. *Coastal Eng. Japan*, 1982, **25**, 125–146.
5. Ting, F. C. K. and Kirby, J. T. Observation of undertow and turbulence in a laboratory surf zone. *Coastal Eng.*, 1994, **24**, 51–80.
6. Ting, F. C. K. and Kirby, J. T. Dynamics of surf zone turbulence in a strong plunging breaker. *Coastal Eng.*, 1995, **24**, 177–204.
7. Ting, F. C. K. and Kirby, J. T. Dynamics of surf-zone turbulence in spilling breaker. *Coastal Eng.*, 1996, **27**, 131–160.
8. Haydon, T. R., Hann, D. B., Davies, P., Greated, C. A. and Barnes, T. C. D. Turbulence structure in surf zone. In *Proc. 25th International Conference on Coastal Engineering*. Orlando, FL, 1996, 214–220.
9. Chang, K.-A. and Liu, P. L.-F. Measurements of breaking waves using particle image velocimetry. In *Proc. 25th International Conference on Coastal Engineering*. Orlando, FL, 1996, 527–537.
10. Deigaard, R., Mikkelsen, M. B. and Fredsoe, J. Measurements of the bed shear stress in the surf zone. *Progress Report*, ISVA, Techn. Univ. Denmark, Lyngby, 1991, **73**, 484–497.
11. Cox, D. T., Kobayashi, N. and Okayasu, A. Bottom shear stress on the surf zone. *J. Geophys. Res.*, 1996, **101**, 14337–14348.
12. Feddersen, F. and Trowbridge, J. H. The effect of wave breaking on surf-zone turbulence and alongshore currents: a modelling study. *J. Phys. Oceanogr.*, 2005, **35**, 2187–2202.
13. Trowbridge, J. H. and Agrawal, Y. C. Glimpses of wave boundary layer. *J. Geophys. Res.*, 1995, **100**, 20729–20743.
14. Feddersen, F. and Williams, A. J. III. A direct estimation of the Reynolds stress vertical structure in the near shore. *J. Atmos. Ocean. Techn.*, 2007, **24**, 102–116.
15. Bryan, K. R., Black, K. P. and Gorman, R. M. Spectral estimates of dissipation rate within and near the surf zone. *J. Phys. Oceanogr.*, 2003, **33**, 979–993.

16. Feddersen, F., Gallagher, E. L., Guza, R. T. and Elgar, S. The drag coefficient, bottom roughness and wave-breaking in the nearshore. *Coastal Eng.*, 2003, **48**, 189–195.
17. Fredsoe, J. and Deigaard, R. *Mechanics of Coastal Sediment Transport*. World Scientific, Singapore, 1992.
18. Songdong Shao. Simulation of breaking wave by SPH method coupled with $k - \varepsilon$ model. *J. Hydr. Res.*, 2006, **44**, 338–349.
19. Lin, P. and Liu, P. L. F. Turbulence transport, vorticity dynamics and solute mixing under plunging breaking waves in surf zone. *J. Geophys. Res.*, 1998, **103**, 15677–15694.
20. Lin, P. and Liu, P. L. F. A numerical study of breaking waves in surf zone. *J. Fluid Mech.*, 1998, **359**, 239–264.
21. Rodi, W. *Turbulence Models and Their Application in Hydraulics*. IAHR, Delft, 1980.
22. Nadaoka, K., Hino, M. and Koyano, Y. Structure of turbulent flow under breaking waves in the surf zone. *J. Fluid Mech.*, 1989, **204**, 359–387.
23. Pedersen, C., Deigaard, R. and Sutherland, J. Turbulence measurements under broken waves. *Progress Report*, ISVA, Techn. Univ. Denmark, Lyngby, 1993, **74**, 81–97.
24. Petti, M. and Longo, S. Turbulence experiments in swash zone. *Coastal Eng.*, 2001, **43**, 1–24.
25. Ting, F. C. K. Laboratory study of wave and turbulence velocities in a broad-banded irregular wave surf zone. *Coastal Eng.*, 2001, **43**, 183–208.
26. Liiv, T. An experimental investigation of the breaking wave characteristics in coastal regions. In *Proc. International Conference on Coastal and Port Engineering in Developing Countries COPEDEC IV*. Rio de Janeiro, 1995, vol. 3, 2334–2343.
27. Liiv, T. Investigation of turbulence in a plunging breaker wave. *Proc. Estonian Acad. Sci. Eng.*, 2001, **7**, 58–78.
28. Stieve, M. J. F. and Wind, H. G. A study of radiation stress and set-up in the nearshore region. *Coastal Eng.*, 1982, **6**, 1–25.
29. Svendsen, I. A. Analysis of surf zone turbulence. *J. Geophys. Res.*, 1987, **92**, 5115–5124.
30. Sakai, T., Mizutani, T., Tanaka, H. and Tada, Y. Vortex formation in plunging breakers. In *Proc. International Conference on Coastal Engineering*. Taipei, Taiwan, 1986, vol. 1, 711–723.
31. Schäffer, H. A., Madsen, P. A. and Deigaard, R. A Boussinesq model for waves breaking in shallow water. *Coastal Eng.*, 1993, **20**, 185–202.
32. Takikawa, K., Yamada, F. and Matsumoto, K. Internal characteristics and numerical analysis of plunging breaker on a slope. *Coastal Eng.*, 1997, **31**, 143–161.
33. Christensen, E. D. and Deigaard, R. Large eddy simulation in breaking waves. *Coastal Eng.*, 2001, **42**, 53–86.
34. Aitsam, A., Daniel, E. and Liiv, U. Investigation of the velocity distribution and shear stresses in decelerated pipe flow. *Proc. Estonian Acad. Sci. Phys. Math.*, 1990, **39**, 290–295.

Murdlaine hüdrodünaamilise kiirusvälja ja kineetilise energia muutumine laine murdepunkti ümbruses

Toomas Liiv ja Priidik Lagemaa

On vaadeldud lainetust lainerennis, mille põhja kalle on $1:17$. Kasutades LDA-mõõtmisi, on uuritud laine perioodi jooksul kahemõõtmelist kiirusvälja, murdlaine kiiruse horisontaal- ja vertikaalkomponendi aegridu ning hetkväärtusi eri ajamomentidel. Kõik mõõtmised on teostatud murdepunkti ümbruses kokku 29 ristlõikes. Mõõtmistulemuste töötlemise põhjal on määratud turbulentse kineetilise energia muutumine risti rannajoonega ja kahemõõtmeline kiiruse vektorväli.